

SOLAR CELLS

Nonalloyed α -phase formamidinium lead triiodide solar cells through iodine intercalation

Yu Zhang^{1†}, Yanrun Chen^{1†}, Guilin Liu², Yuetong Wu¹, Zhenyu Guo¹, Rundong Fan¹, Kailin Li¹, Huifen Liu¹, Yeping Zhao³, Tim Kodalle^{4,5,6}, Yihua Chen⁷, Cheng Zhu⁷, Yang Bai⁷, Qi Chen⁷, Huanping Zhou^{1,8,9*}

Formamidinium lead triiodide (FAPbI_3) is considered the most promising composition for high-performing single-junction solar cells. However, nonalloyed α - FAPbI_3 is metastable with respect to the photoinactive δ -phase. We have developed a kinetic modulation strategy to fabricate high-quality and stable nonalloyed α - FAPbI_3 films, assisted by cogenetic volatile iodine intercalation and decalculation. The intercalation of iodine facilitated the formation of corner-sharing Pb-I framework building blocks and reduced the kinetic barrier for α - FAPbI_3 formation, whereas the iodine decalculation improved the final perovskite film quality in terms of composition purity and overall homogeneity. Solar cells based on this nonalloyed α - FAPbI_3 (free of other extrinsic composition ions) achieved a power conversion efficiency of >24%. The devices also exhibited excellent durability, retaining 99% of their original power conversion efficiency after operating for more than 1100 hours at $85^\circ \pm 5^\circ\text{C}$ under illumination.

Perovskite solar cells (PSCs) have demonstrated exceptional power conversion efficiency (PCE) and low manufacturing costs (1–4), but the poor long-term stability of PSCs hampers their commercialization. Additive engineering, interface engineering, and transport layer design have extended the operational life-span of PSCs to several thousand hours, but the intrinsic instability of hybrid perovskite absorber is still the major obstacle in their potential for full commercial deployment (5). Formamidinium lead triiodide (FAPbI_3) has been considered the most competitive absorber for single-junction PSCs but suffers from complex crystallization kinetics and thermodynamic metastability, and preparing nonalloyed and high-quality α - FAPbI_3 perovskite films has proven difficult (6). Challenges include high nucleation barriers of α - FAPbI_3 when compared with non-photoactive δ - FAPbI_3 , mass-transfer limitations of FAI, and sensitivity to moisture associated with the α -phase degradation that often leads to films with low crystal quality and poor stability (7, 8).

Kinetic modulation of the perovskite crystallization process can effectively mitigate these

issues. This can be achieved by regulating intermediate structures through ammonium cation alloying [such as methylammonium (MA^+), thiophenemethylammonium (TMA^+), and propylammonium (PA^+)] (9–11) and halide or pseudo-halide doping [such as Cl^- , thiocyanate (SCN^-), and acetate (Ac^-)] (12–14), as well as by templating growth with seed crystals that have suitable lattice structures, such as two-dimensional (2D) perovskites (15–18). However, these methods often introduce extra instability factors in FAPbI_3 through the presence of residual compositional additives that may cause cation–anion segregation (e.g., FA^+/MA^+ , I^-/Cl^-) (19, 20), thermal decomposition (such as MA^+) (21), and even nucleophilic reactions between FA^+ and Lewis base species (such as ammonium groups) (22–25). Moreover, fabrication techniques such as solvent annealing, moisture-induced phase transitions, and infrared thermal annealing used to produce pure α - FAPbI_3 by alleviating lattice strain (26–28) can lead to unsatisfactory performance compared with alloyed perovskites, likely because of their poorer film quality.

Here, we describe an iodine intercalation-decalculation strategy to fabricate high-quality, nonalloyed α - FAPbI_3 perovskite films. The cogenetic volatile additive, iodine (I_2), altered the reaction pathway by reacting with iodide ions to form polyiodides such as I_3^- , and in particular the perovskite-iodine complex intermediate. These intermediates provided sufficient corner-sharing Pb-I framework building blocks for α - FAPbI_3 perovskite formation and reduced the reaction activation energy. Upon annealing, iodine could escape from the final film without residual additives to yield films with enhanced uniformity and crystal quality. Solar cells incorporating this nonalloyed α - FAPbI_3 had PCEs >24%. Moreover, the modified PSCs demonstrate excellent operational stability and

maintained 99% of their initial PCE after operation for 1180 hours (100 mW cm^{-2} , 85°C). This study highlights the importance of nonalloyed FAPbI_3 (free of other ions such as MA^+ , Cs^+ , Br^- , and SCN^-) for the intrinsic stability of perovskite materials and sheds light on how iodine chemistry dynamically modulates the formation path of metastable perovskites and other optoelectronic materials with a soft ionic lattice.

Design and validation of chemical strategies for nonalloyed α - FAPbI_3

The composition and crystalline quality collectively determine the intrinsic properties of perovskites. Despite the extensive adoption of various alloyed perovskites ($\text{FA}_{1-x-y}\text{MA}_x\text{Cs}_y\text{PbI}_{1+x+y}\text{Br}_z\text{Cl}_j$) compositions in PSCs, their inherent thermodynamic instabilities, such as the thermal decomposition of MA^+ , segregation at the A/X sites, and irreversible ion migration, necessitate the exploration of more advanced material composition (Fig. 1A, left). In this context, the FAPbI_3 -based composition has markedly improved thermal stability compared with MA-contained perovskite. To obtain high-quality FAPbI_3 thin films, ionic additives like MACl are typically used to enhance crystallinity (Fig. 1A, center). However, although these perovskites are often described as “pure FAPbI_3 ,” they actually contain a considerable amount of thermally unstable MA^+ cations, which is ~5%, as confirmed by nuclear magnetic resonance (NMR) data reported in the literature (29) and our studies, that negatively affects their long-term stability.

High-quality nonalloyed FAPbI_3 films (Fig. 1A, right) can effectively mitigate the inherent instability issues associated with alloyed perovskites. Accordingly, we developed a reaction pathway modulation strategy assisted by an optimal volatile additive that enhanced reactivity with AX or BX₂ compounds to promote α - FAPbI_3 formation, inhibited formation of the δ -phase, and also completely escaped from the film during postannealing. After finely screening several possible additives, such as organic molecules and halides, we identified the cogenetic iodine (I_2) as the best candidate. Not only does it have high reactivity and volatility (30, 31), I_2 is also a Lewis acid that has strong bonding capacity with I^- (a Lewis base) to form polyiodide ions such as I_3^- , which shifted the reaction path from $\text{FAI} + \text{PbI}_2 \rightarrow \text{FAPbI}_3$ to $\text{FAI}_3 + \text{PbI}_2 \rightarrow \text{FAPbI}_3 + \text{I}_2$.

Moreover, I_2 is considered a cogenetic volatile molecule that ensures the absence of any extrinsic residue in the film to contribute to composition purity of FAPbI_3 (fig. S1). Given the substantial ionic size of polyiodides, they are more likely to decorate on the surface of intermediate clusters instead of incorporating into the lattice. This intermediate could be expected to regulate the reaction pathway from

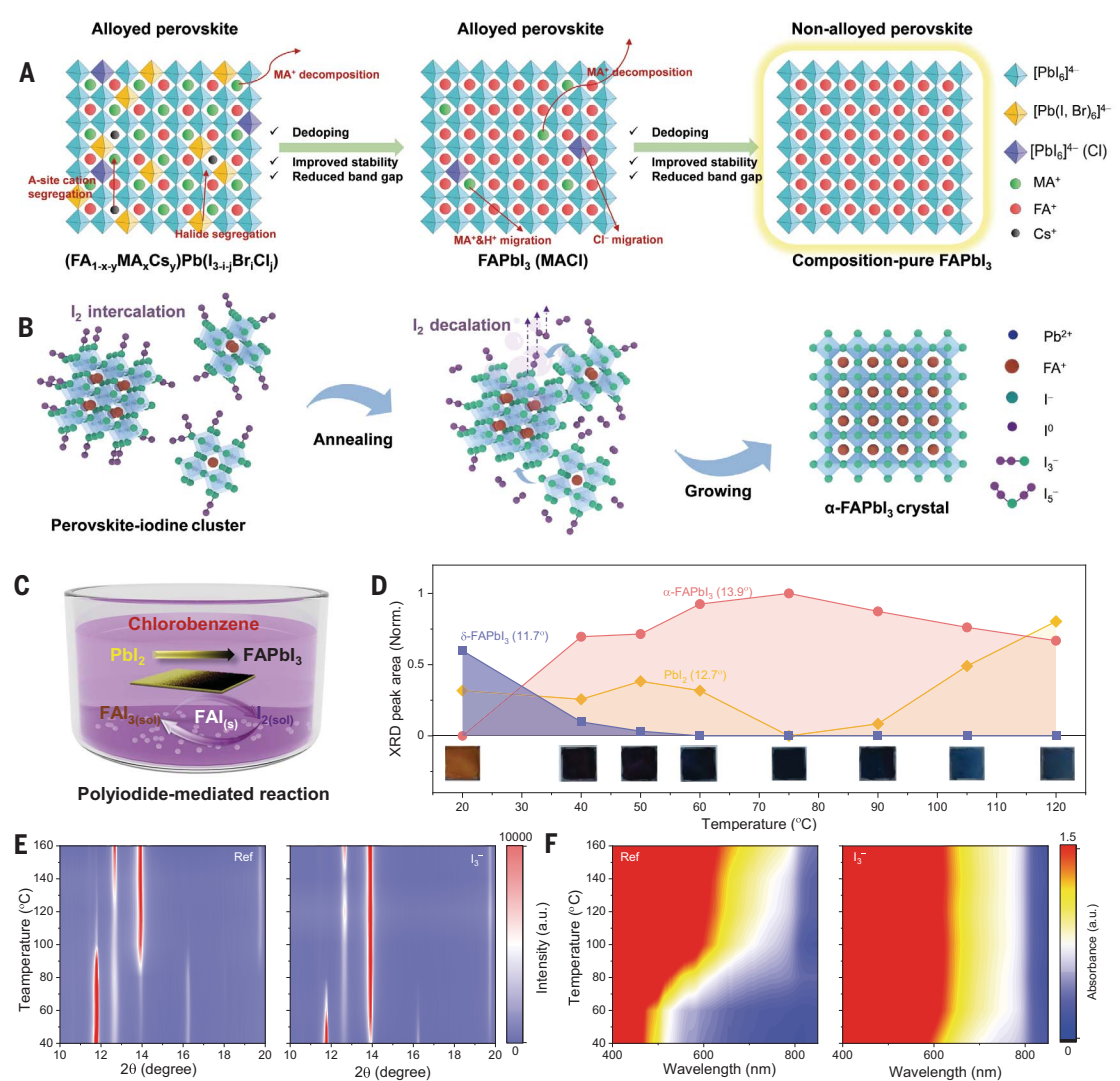
¹Beijing Key Laboratory for Theory and Technology of Advanced Battery Materials, Key Laboratory of Polymer Chemistry and Physics of Ministry of Education, School of Materials Science and Engineering, Peking University, Beijing, P. R. China. ²School of Science, Jiangnan University, Wuxi, Jiangsu, P. R. China. ³Department of Materials Science and Engineering, University of California Los Angeles, Los Angeles, CA, USA. ⁴Molecular Foundry, Lawrence Berkeley National Laboratory, Berkeley, CA, USA. ⁵Advanced Light Source, Lawrence Berkeley National Laboratory, Berkeley, CA, USA. ⁶Materials Science Division, Lawrence Berkeley National Laboratory, Berkeley, CA, USA. ⁷School of Materials Science and Engineering, Beijing Institute of Technology, Beijing, P. R. China. ⁸Institute of Carbon Neutrality, Peking University, Beijing, P. R. China. ⁹Southwest United Graduate School, Kunming, P. R. China.

*Corresponding author. Email: happy_zhou@pku.edu.cn

†These authors contributed equally to this work.

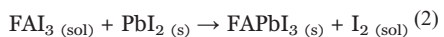
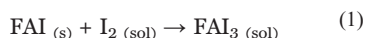
Fig. 1. Design principle and proof of concept for iodine-mediated formation of nonalloyed α -FAPbI₃.

(A) Schematics of nonalloyed perovskite component design and advantages. (B) Schematics of mechanism for iodine-mediated formation of α -FAPbI₃. (C) Schematics of α -FAPbI₃ converted from PbI₂ films immersed in CB with soluble iodine and FAI solids. (D) Integration of α -FAPbI₃, δ -FAPbI₃, and PbI₂ XRD peak areas at different reaction temperatures. (E) XRD patterns for FAI (left) or FAI + I₂ (right) spin-coated on PbI₂ films as a function of annealing temperature. (F) UV-vis absorption spectra for FAI (left) or FAI + I₂ (right) spin-coated on PbI₂ films as a function of annealing temperature.



PbI₂ to FAPbI₃, thereby altering the energy barrier and lattice rearrangement for perovskite formation (Fig. 1B). Upon annealing, the polyiodides decompose into gaseous I₂, which aids in the seamless integration and growth of these clusters into high-quality nonalloyed FAPbI₃ films.

We first explored the feasibility of the iodine intercalation-decalation strategy to promote α -FAPbI₃ formation in solution (Fig. 1C). Polyiodides are generated when I₂ reacts with I⁻ ions (for example, I₂ + I⁻ → I₃⁻) in various solvents, as verified by Raman spectra (fig. S2). We chose chlorobenzene (CB) as the ideal solvent to specify the reactivity of polyiodides because CB can only dissolve polyiodides (such as I₃⁻) but not the hydrophilic iodides (I⁻). When immersing a PbI₂ film in a CB solution containing soluble I₂ and excess FAI powder, it undergoes reactions (1) and (2):



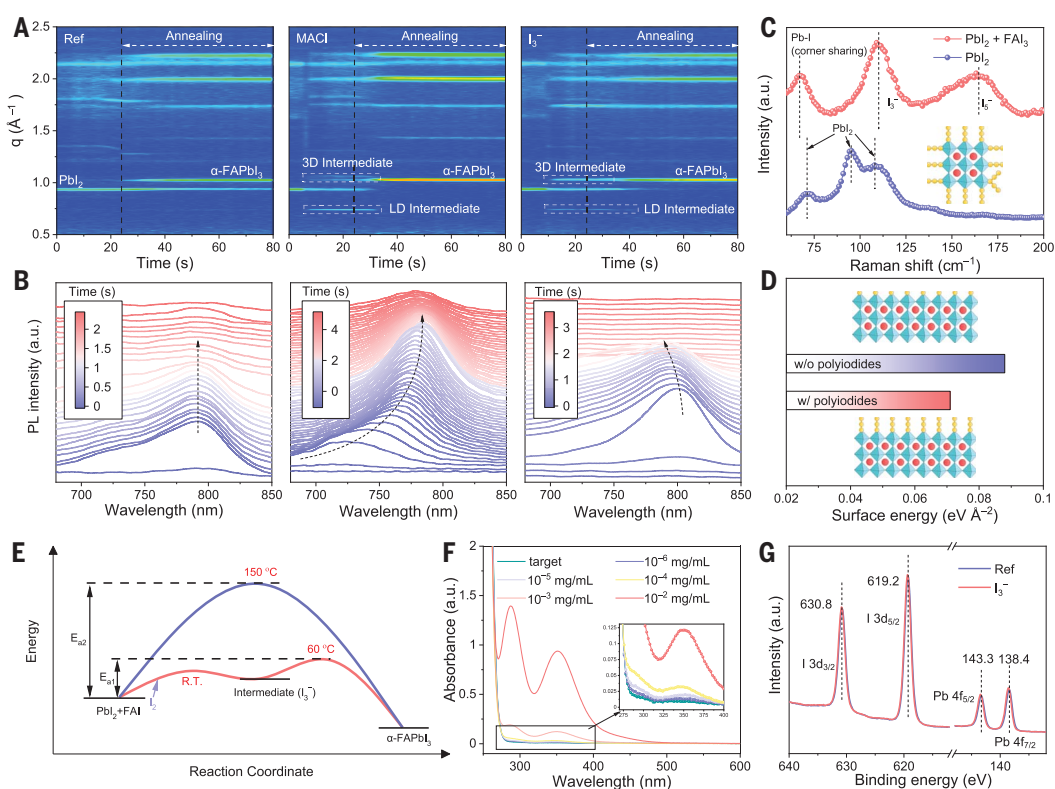
By systematically adjusting the temperature, we observed that the transformation temperature from yellow PbI₂ to black perovskite occurred only above 40°C (Fig. 1D, inset images), which suggested that the polyiodide can serve as the reactant during the formation of α -FAPbI₃. We performed x-ray diffraction (XRD) measurements on the treated films between 20° and 120°C (near the boiling point of CB) and integrated the characteristic peak of the PbI₂, α -FAPbI₃, and δ -FAPbI₃ phases (Fig. 1D and fig. S3). At room temperature, the δ -FAPbI₃ peak (11.7°) appeared after the film was immersed for 12 hours. As the temperature increased, the intensity of the δ -phase gradually diminished, whereas that of the α -phase (13.9°) increased.

Notably, the δ -phase peak completely disappeared above 60°C, indicating a direct transformation from PbI₂ to α -FAPbI₃. This transformation occurred at a much lower temperature than the typical requirement of >150°C for α -FAPbI₃ formation, suggesting that iodine and the as-formed polyiodides facilitated an effective reaction pathway. By contrast, reac-

tions between PbI₂ and FAI conducted in isopropanol (IPA) solution resulted in negligible perovskite formation, illustrating that the barrier to perovskite formation is substantially higher without polyiodide mediation (fig. S4). Additionally, the chemical equilibrium between PbI₂ and α -FAPbI₃ is discussed in fig. S5 and supplementary text S1.

We further investigated the efficacy of iodine intercalation-decalation reactions with the assistance of the commonly used two-step approach to form FAPbI₃ films. For clarity, the samples without any additives were referred to as “Ref” sample, and those with polyiodides were labeled as “I₃⁻” sample, respectively. Noticeable differences in color and texture between the two unannealed precursor films were observed; the Ref film appeared yellow and rough with the precipitation of snowflake-like FAI crystals on the PbI₂ surface, whereas the I₃⁻ film was brown and exhibited a smooth surface (fig. S6). These results demonstrated that polyiodides enhanced the reactivity between FAI and PbI₂ at room temperature.

Fig. 2. Mechanism of iodine-mediated FAPbI₃ film formation. (A) In situ GIWAXS of Ref, MACl, and I₃⁻ samples during spin coating and annealing at 120°C. (B) In situ PL spectra of Ref, MACl, and I₃⁻ samples during spin coating. (C) Raman spectra of PbI₂ and polyiodide-coordinated perovskite intermediate. (D) Calculated surface energies of perovskite clusters with or without polyiodides. (E) Scheme of energy variation as a function of reaction coordinate for the reaction FAI + PbI₂ → FAPbI₃ with or without polyiodides. (F) UV-vis absorption spectra of potential residual I⁰ dissolved in aqueous solution from perovskite, compared with the absorption spectra of I⁰ solutions at quantified concentrations. (G) XPS spectra of Pb 4f and I 3d of perovskite films.



We subsequently examined the perovskite film properties as a function of annealing temperatures using XRD and ultraviolet-visible (UV-Vis) absorption spectroscopy measurements. The XRD pattern showed that in the Ref samples, the δ -FAPbI₃ peak (11.7°) was detectable within room temperature to 150°C, consistent with literature reports (Fig. 1E) (27). Conversely, in I₃⁻ samples, the δ -FAPbI₃ signals vanished at relatively low temperature of 80°C, which was almost consistent with the above experiments (Fig. 1, C and D). Polyiodides appeared to prevent secondary phases formation and lowered the formation barrier for the α -FAPbI₃. Temperature-dependent absorption spectra further confirmed this phenomenon (Fig. 1F), in which the absorption signals at 600 to 820 nm corresponding to photoactive α -FAPbI₃ were maximized at 150° and 80°C for Ref and I₃⁻ sample, respectively.

Mechanisms of iodine-mediated reaction

To investigate the microstructural phase evolution upon the reaction between PbI₂ films and FAI solution with different additives, we conducted in situ grazing-incidence wide-angle x-ray scattering (in situ GIWAXS). Here, we introduced a FAI solution containing the commonly used additive MACl to form the alloyed FAPbI₃(MACl) film as an additional reference (labeled as “MACl” sample, Fig. 2A). In the Ref sample, almost no signal of perovskite intermediate was observed, whereas that of PbI₂ ($q = 0.92 \text{ \AA}^{-1}$, where q is the scattering vector)

was unchanged during spin coating before annealing. These results suggested that the FAI diffusion into the PbI₂ film was substantially blocked without any additives, which aligned with the above findings (fig. S6) and also previous work (32). By contrast, in the MACl samples, we observed the formation of three-dimensional (3D) intermediates at $q = 1.03$ and 1.06 \AA^{-1} during spin coating, which can be referred to as FAPbI₃(MACl) species with different relative amounts of MACl. Simultaneously, another low-dimensional (LD) intermediate appeared at $q \approx 0.73 \text{ \AA}^{-1}$ in the MACl sample, which was reported as AX-rich perovskite, such as (FAI)_xFAPbI₃ (33).

The I₃⁻ sample also showed 3D and LD intermediates at scattering vector $q = 1.03$ and 0.73 \AA^{-1} , respectively, where the former could be attributed to perovskite intermediate involved with I₃⁻ and the latter to LD intermediates. Thus, polyiodides could alter the reaction pathway and enhance the reactivity between FAI and PbI₂, similar to that of the MACl additive. We showed a speculated distribution of each intermediate species in the film before annealing in fig. S7. In brief, both the I₃⁻ and MACl samples formed 3D and LD intermediates, whereas the Ref sample displayed negligible reactivity between PbI₂ and FAI. After annealing at 120°C, the intermediate phases of the I₃⁻ and MACl samples rapidly converted to perovskite within ~10 s, whereas the Ref still retained a certain fraction of unreacted PbI₂.

We used in situ photoluminescence (in situ PL) to track the perovskite intermediate evolu-

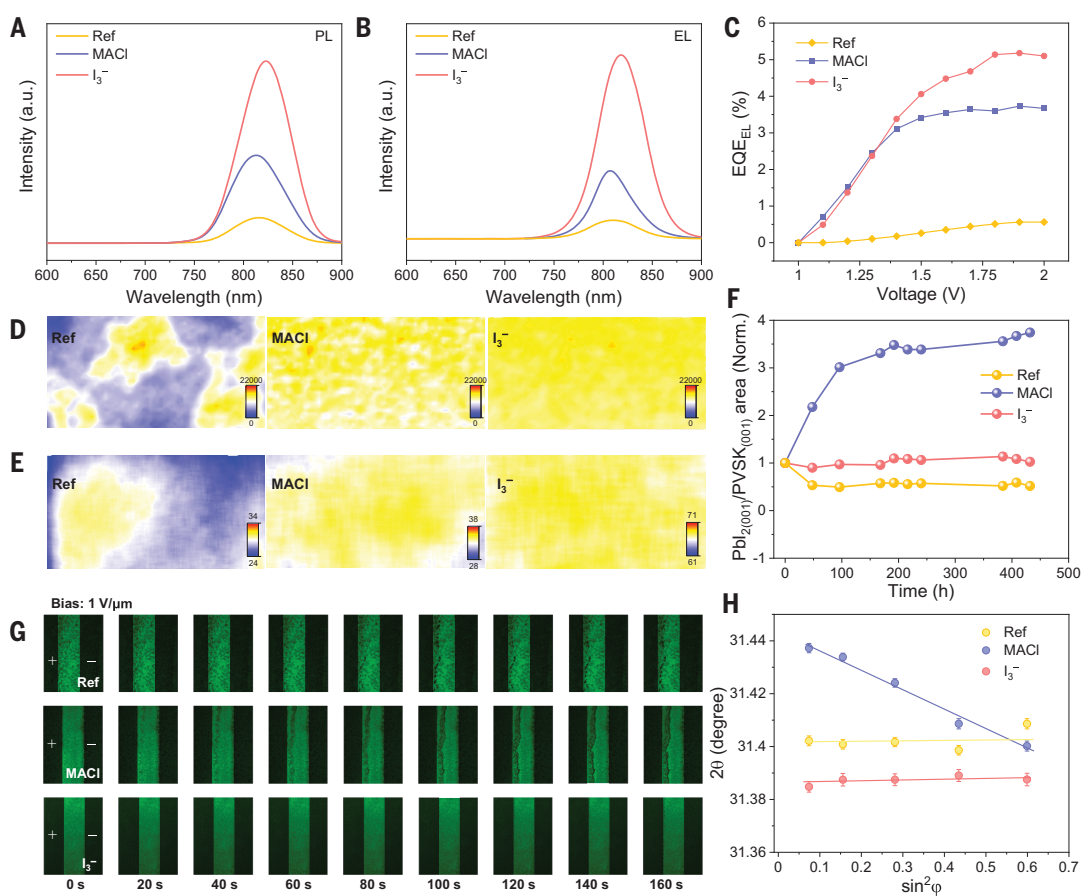
tion during spin coating (Fig. 2B). The Ref film exhibited a weak PL peak with a fixed wavelength (790 nm), indicating the formation of only traces of the photoactive perovskite phases. For the MACl sample, the PL peak exhibited a gradual shift from 720 to 780 nm, which indicated the formation of the intermediate composition. Rapid perovskite nucleation would incorporate MACl, and subsequent substitution of FAI into the lattice would reduce the bandgap and red-shift the PL peak.

By contrast, the PL peak of I₃⁻ sample blue-shifted from 800 to 785 nm, suggesting the formation of different intermediate structures than in the case of the MACl sample (supplementary text S2). Raman spectra of the I₃⁻ sample showed both polyiodide (I₃⁻ and I₅⁻) and corner-sharing Pb-I bond signals (31, 34) (Fig. 2C) indicative of polyiodide-coordinated intermediate clusters. The peak positions of I₃⁻ and I₅⁻ polyiodide ions shifted toward higher frequencies by 2 and 5 cm⁻¹, respectively, compared with those in FA-salt films, highlighting interactions between the polyiodide ions and the Pb-I framework (fig. S8) in the I₃⁻ sample.

The reaction of I₂ as a Lewis acid with I⁻ as a Lewis base to form I₃⁻ is spontaneous at room temperature (35). Moreover, I₃⁻ contains two I-I bonds, each with a bond length of ~0.3 nm, versus the ionic radius of I⁻ of ~0.21 nm, and it is difficult to incorporate such a large ion into the bulk lattice of the perovskite. Thus, in the perovskite precursor film, I₂ should

Fig. 3. Film quality and stability.

PL spectra (**A**) of perovskite films and EL spectra (**B**) of PSCs. (**C**) EQE_{EL} measurements of the devices under bias from 1 to 2 V. PL intensity mapping (**D**) and TRPL mapping (**E**) of perovskite films. (**F**) Evolution of the ratio between PbI₂ and perovskite (001) peak intensity in XRD patterns of Ref, MACl, and I₃⁻ films during aging at 85 °C. (**G**) PL images of ITO/perovskite/ITO devices under a constant applied bias (1 V/μm). The bright areas represent PL emission from the perovskite films. (**H**) Linear fit of $2\theta \cdot \sin^2 \varphi$ for residual stress in perovskite films, where 2θ stands for diffraction angle and φ stands for the angle between the diffraction vector and the sample normal direction.



combine with unsaturated I⁻ on the perovskite intermediate surface to form I₃⁻ and create clusters of perovskite intermediates coordinated by I₃⁻, namely FAPbI₃(I₃⁻) (Fig. 2C, inset).

We used density functional theory (DFT) calculations to gain insights into the polyiodide-mediated process. Surface-coordinated polyiodides could reduce the surface energy of the system by 20%, from 0.088 to 0.071 eV Å⁻² (Fig. 2D). Such a modified surface would contribute to a reduction in the overall Gibbs energy of the perovskite intermediate, thereby regulating the reaction pathway and lowering the formation barrier of the α-FAPbI₃. In summary, the polyiodides-assisted approach greatly reduced the α-FAPbI₃ formation temperature, suggesting much lower activation energy (E_{al}) associated with the low-surface energy intermediates, FAPbI₃(I₃⁻). A schematic energy diagram of FAPbI₃ formation kinetics mediated by polyiodides is illustrated in Fig. 2E.

Additionally, we assessed the amount of residual I⁰ to determine whether polyiodides fully decomposed and escaped during annealing. The UV-vis analysis revealed that, despite the high initial concentration of elemental iodine in the precursor solution (I⁰/FAI = 27%), the

residual amount of I⁰ was less than 0.00001% (Fig. 2F and supplementary text S3). We also analyzed the surface of perovskite films using x-ray photoelectron spectroscopy (XPS) to determine the presence of any residual coordinated I⁰ (Fig. 2G). In Ref and I₃⁻ films, the binding energy (BE) at 143.32 and 138.40 eV was assigned to 4f_{5/2}, 4f_{7/2} of divalent Pb²⁺, and the BE at 630.81 and 619.20 eV was assigned to 3d_{3/2}, 3d_{5/2} of monovalent I⁻, respectively. The I₃⁻ films showed an equal intensity of signals for I⁻ compared with Ref films, without any shoulder peaks of I⁰ at higher BE, indicating that I⁰ had entirely escaped from the perovskite system after annealing.

Purity, uniformity, and stability of nonalloyed FAPbI₃ films

Compositional purity is crucial for metal halide perovskite for practical use. Accordingly, we evaluate the purity of annealed FAPbI₃ films fabricated with different precursors. Time-of-flight secondary ion mass spectrometry (TOFSIMS) depth profile analysis of different FAPbI₃ perovskite films revealed that the MA and Cl (fig. S9) signals could be detected in the MACl sample, suggesting that the thermally unstable MACl component remained in the perovskite film.

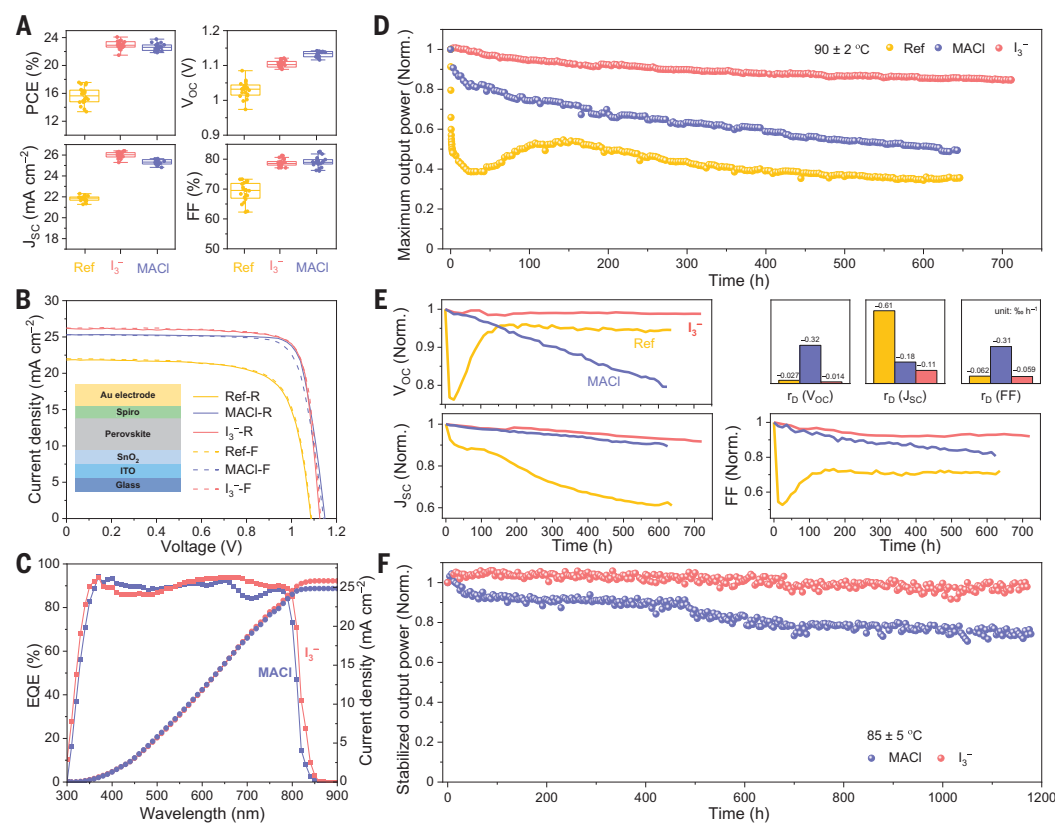
We further quantified the composition of the perovskite using ¹H nuclear magnetic resonance (NMR) by dissolving it in deuterated dimethyl sulfoxide (DMSO-*d*₆) (fig. S10). Integration of the FA⁺ and MA⁺ resonances in the quantitative ¹H spectrum yielded a concentration of MA⁺ in the final film of ~5% in MACl films, which was consistent with previous work (29). By contrast, both TOFSIMS profiles and NMR spectra results showed that the signals of I₃⁻ sample were similar to those of Ref, as no extrinsic ions such as MA⁺, Cs⁺, and Br⁻ were introduced.

The steady-state PL of the I₃⁻ sample was notably higher than that of Ref and MACl (Fig. 3A). This result suggested that the iodine-mediated perovskite crystal quality was enhanced and nonradiative recombination was suppressed, which was also supported by PL mapping results (Fig. 3D). The PL peak of the I₃⁻ sample was located at 823 nm, which was red-shifted compared with that of the Ref (816 nm) and MACl (812 nm) samples. This red-shift could be attributed to the superior crystal quality (compared with Ref) and purer components (compared with MACl sample) present in the I₃⁻ sample.

To further evaluate the optoelectronic properties and defect behavior of FAPbI₃ films, we

Fig. 4. Device performance.

(A) Statistics of PCE, V_{OC} , J_{SC} and FF based on 20 individual devices. Plots of the box-chart graphs containing the mean value, maximum and minimum values, bounds of box, whiskers, and percentile. **(B)** $J-V$ curve of the champion devices under both reverse and forward voltage scans (the inset shows the device structure). **(C)** Incident photon-current efficiency spectra together with the integrated J_{SC} for the I_3^- and MACI device. **(D)** Evolution of the normalized power output of unencapsulated Ref, I_3^- , and MACI device (PTAA HTLs) under continuous light irradiation and MPP tracking at $90 \pm 2^\circ\text{C}$ in a nitrogen glovebox. **(E)** The evolution of V_{OC} , J_{SC} , FF and their fitting degradation rate (r_D) under MPP tracking. **(F)** Evolution of the normalized power output of unencapsulated I_3^- and MACI device (PDCBT/PTAA HTLs) under continuous light irradiation and stabilized power-output tracking with a full-spectrum halogen lamp (100 mW cm^{-2}) at $85^\circ \pm 5^\circ\text{C}$ in a nitrogen glovebox.



fabricated devices with the structure of ITO/SnO₂/perovskite/Spiro-OMeTAD/Au {where ITO is indium tin oxide and Spiro-OMeTAD is 2,2'7,7'-tetrakis[N,N-bis(p-methoxyphenyl)amino]-9,9'-spirobifluorene}. Current injection allowed the devices to operate as light-emission diodes (LEDs) and revealed electroluminescence (EL) peaks for the I_3^- sample, Ref sample, and the MACI sample located at 819, 811, and 808 nm (Fig. 3B), respectively. These positions and intensities were consistent with the trend observed in steady PL. The I_3^- sample demonstrated the longest wavelength of EL emission among perovskite LEDs based on FAPbI₃ among reported devices (table S1). The maximum external quantum efficiency (EQE) of EL reached 5.18% for the I_3^- device at 1.9 V bias voltage (Fig. 3C), whereas the MACI and Ref devices obtained EQEs of only 3.73 and 0.59%, respectively. Thus, I_3^- inhibited nonradiative combination as well as open-circuit voltage (V_{OC}) loss, according to the equation $V_{OC,loss} = -k_B T/e \ln \text{EQE}_{EL}$, where k_B is the Boltzmann constant, T is the temperature, and e is the electronic charge.

We characterize film uniformity in terms of morphology and optoelectrical properties. In scanning electron microscope (SEM) images, Ref exhibited an uneven spatial grain size distribution ranging from 300 nm to 1 μm , which probably related to the limited diffusion capacity of FAI that resulted in different

nucleation rate. By contrast, both MACI- and I_3^- -mediated perovskite exhibited enhanced uniformity with an average grain size of ~1 μm and ~600 nm (fig. S11), respectively, that may reflect effective coarsening of grains.

We also performed PL-mapping measurements on 25- μm by 12.5- μm regions in the films (Fig. 3D). The Ref film showed substantial variation of PL intensity, where the dark region size was consistent with that of the domains observed in SEM images. Compared with the Ref and MACI samples, the variations in PL intensities were notably reduced in the I_3^- sample, indicating its uniform composition and phase distribution. To further investigate the uniformity of carrier lifetime across the films, we performed time-resolved PL (TRPL) mapping over a 10- μm by 5- μm region (Fig. 3E). The overall lifetime of I_3^- samples (average 67 ns) was higher than that of Ref (28 ns) and MACI (34 ns), and the lifetime distribution of I_3^- was concentrated in the range from 65 to 68 ns, whereas the Ref sample exhibited a broader distribution of 24 to 32 ns.

To investigate the stability of FAPbI₃ perovskite during the aging process, we also characterized the corresponding phase and optoelectronic property evolution. Perovskite films were subjected to thermal stability testing at 85°C, and the decomposition or phase transition of perovskite were analyzed by XRD measurement

(Fig. 3F and fig. S12). During the first 48 hours, Ref films showed a decreased peak intensity of PbI₂, along with increased perovskite (001) peak intensity, indicating extended reaction between unreacted PbI₂ and FAI residues. Subsequently, the signals of PbI₂ and perovskite were unchanged. In MACI films, the peak intensity of PbI₂ gradually increased during aging over 480 hours, indicating continuous degradation of the MACI sample caused by the thermal decomposition of residual MACI and subsequent formation of PbI₂. Similarly, the PL red-shifted from 812 to 820 nm as the perovskite composition changed from FA_{1-x}MA_xPbI₃ to FAPbI₃ that had a lower bandgap (fig. S13).

In comparison, the I_3^- films showed no obvious change of PbI₂ and perovskite signal, with a constant PbI₂/perovskite ratio throughout the entire test. The thermal stability of the composition-pure FAPbI₃ was further confirmed by steady-state PL (fig. S13), where no obvious shift was observed in PL peaks of I_3^- films. Thermogravimetric analysis (fig. S14) also confirmed that the MACI film had ~1% mass loss below 200°C, whereas there was no mass loss in the I_3^- film.

To characterize ion migration in a perovskite film under an applied electric field, we established a vertical setup (ITO/FAPbI₃/Au) to measure bias-modulated PL. In MACI devices, PL intensity dropped to 85% of the initial value

in 150 s (fig. S15) after applying a voltage of 1.1 V, indicating that ion migration would induce excess defects in the film and thus more nonradiative combination. However, PL intensities in the Ref and I_3^- devices were stable throughout the same tests, showing that composition-pure FAPbI₃ films inhibited ion migration compared with FAPbI₃ doped with MACl.

We further characterized the PL of perovskite thin films between two in-plane electrodes, with a constant electrical bias (1 V/ μ m) applied, to examine the field-induced ion migration in perovskite films. In a series of PL images of the films as a function of time (Fig. 3G), we observed PL quenching near the electrode for the MACl film in the initial 40 s. Defects likely accumulated in these regions under the electrical field and suppressed PL. The quenching behavior in the Ref film appeared after 80 s. For the I_3^- film, the PL region showed almost no change throughout the entire measurement, indicating that ion migration in composition-pure FAPbI₃ films was greatly suppressed.

We also investigated in-plane residual strain in FAPbI₃ films using grazing-incident x-ray diffraction. By fitting the 2θ as a function of $\sin^2\varphi$, we calculated the slope of the fitting line that stood for the residual strain (36). The negative slope of the fitting line indicated that the MACl film exhibited the tensile strain, whereas the Ref and I_3^- films showed a negligible strain (Fig. 3H). Tensile strain can be induced by vertical distribution of MA⁺, in that MA⁺ is prone to remaining in the surface and causing the lattice constant to decrease from the bottom of the film to the surface. Residual tensile strain can negatively affect the device interfacial carrier transport and photovoltaic performance. In comparison, the Ref and I_3^- films ensured the composition distribution homogeneity by virtue of composition purity and thus eliminated in-plane residual strain.

Device performance

We investigated the performance of the corresponding PSCs using an ITO/SnO₂/perovskite/Spiro-OMeTAD/Au configuration. The optimized I_3^- devices, fabricated with a precursor containing 100 mM I₂ (fig. S16), showed improved photovoltaic performance compared with Ref (Fig. 4A). Mainly, the average PCE increased from 15.6 to 22.9%, the V_{OC} from 1.04 to 1.11 V, the short-circuit current density (J_{SC}) from 21.9 to 26.0 mA cm⁻², and the fill-factor (FF) from 70.3 to 79.1%, respectively. Furthermore, the average PCE of I_3^- devices was comparable with that of MACl devices (22.9% versus 22.6%), along with a higher J_{SC} (26.0 mA cm⁻² versus 25.3 mA cm⁻²) and a lower V_{OC} (1.11 V versus 1.13 V), which could be attributed to the lower bandgap of I_3^- films. Moreover, the performance of I_3^- devices exhibited good reproduc-

ability across different experimental batches (fig. S17).

The champion I_3^- device yielded a PCE of 24.1% with a J_{SC} of 26.25 mA/cm², a V_{OC} of 1.13 V, and a FF of 81.2% (Fig. 4B). The stable output at the maximum power point (MPP) of 0.99 V of the device was 24.1% (fig. S18). Integrating the incident photon-current efficiency spectrum of I_3^- PSC delivered a 25.8 mA cm⁻² current density (Fig. 4C), substantially surpassing the 24.8 mA cm⁻² observed in the MACl device. We note that the PCEs of FAPbI₃ PSCs without any ionic additives were all <22%, whereas the present I_3^- device achieved a PCE surpassing 24%, which exceeded previous PCEs reported for composition-pure FAPbI₃ PSCs. Higher PCEs of I_3^- cells, particularly the V_{OC} and FF, could result from improvements in interface energy alignment and carrier transport. Further investigations confirmed that our strategy can also enhance device performance in the one-step fabrication method (fig. S19 and supplementary text S4). In addition, the synergistic effect of iodine and other ionic additives was explored (fig. S20).

The operational stability of PSCs was assessed by exposing unencapsulated devices to continuous illumination (100 mW cm⁻²) with MPP tracking at a steady temperature of 90° ± 2°C (Fig. 4D). By replacing the hole-transport layer (HTL) Spiro-OMeTAD with a thermally stable conductive polymer poly[bis(4-phenyl)(2,4,6-trimethylphenyl)amine] (PTAA), the initial PCEs for the I_3^- , MACl and Ref devices were 22.1, 20.1, and 16.3%, respectively (fig. S21). The I_3^- device maintained >85% of its initial PCE after 712 hours, substantially surpassing the Ref and the MACl devices, which preserved only 36 and 49% of their PCEs after 642 hours, respectively.

We also monitored the evolution of V_{OC} , J_{SC} , and FF for these devices during aging by conducting $J-V$ scans at 12-hour intervals (Fig. 4E) and further quantified the degradation rate (r_D) of various parameters over time through linear fitting. The Ref device showed low degradation rates of -0.027%/hour and -0.062%/hour for V_{OC} and FF, respectively, whereas a rapid decay rate of -0.61%/hour for J_{SC} indicated progressive degradation of photoactive regions in low-quality Ref perovskite. The I_3^- cell demonstrated the lowest degradation rates for V_{OC} , J_{SC} , and FF, at -0.014, -0.11, and -0.059%/hour, respectively. In stark contrast, the MACl devices showed V_{OC} and FF degradation rates that were higher than those of the nonalloyed Ref and I_3^- devices, at -0.32 and -0.31%/hour, respectively.

We further introduced a poly[5,5'-bis(2-butyloctyl)-(2,2'-bithiophene)-4,4'-dicarboxylate-alt-5,5'-2,2'-bithiophene] (PDCBT) interlayer to mitigate the adverse effects of dopants in PTAA on the perovskite and assessed the stability of both I_3^- and MACl devices. The initial PCEs

for the I_3^- and MACl devices with a PTAA/PDCBT HTL were 20.7 and 18.7%, respectively (fig. S22). The MACl cells underwent a 20% reduction in PCE after operation for 1180 hours at 85° ± 5°C. Conversely, the I_3^- cell maintained 99% of its initial PCE under the same continuous operating conditions (Fig. 4F), demonstrating state-of-the-art operational stability for PSCs.

Additionally, we explored the potential of our approach in p-i-n devices. By using [4-(3,6-dimethyl-9H-carbazol-9-yl)butyl]phosphonic acid (Me-4PACz) or PTAA as the HTL, we achieved a device PCE of 24.0 and 23.1%, respectively, by using the ITO/HTL/ I_3^- perovskite/C₆₀/BCP/Au configuration (fig. S23). Devices equipped with the ITO/PTAA/perovskite/C₆₀/SnO₂/ITO/Au configuration maintained 99% of the initial PCE after operating at 85°C for 622 hours (fig. S24). We sent encapsulated p-i-n devices to a third-party organization (National Center of Inspection on Solar Photovoltaic Products Quality, CPVT) for damp heat (DH) and thermal cycling (TC) tests (figs. S25 to S27). The certificate confirmed that our devices exhibited no degradation after enduring 500 hours of DH and 300 cycles of TC testing, underscoring their robustness.

Discussion

We demonstrate a strategy for modulating crystallization kinetics to fabricate stable nonalloyed α -FAPbI₃ perovskite films with high crystal quality by cogenetic volatile iodine intercalation and decalation. I₂ and as-formed polyiodides facilitate the nucleation of corner-sharing lead iodide frameworks, effectively reducing the kinetic barrier for α -FAPbI₃ formation. And the complete sublimation of iodine during annealing ensures the final perovskite film quality in terms of composition purity and overall homogeneity. On the basis of the resultant nonalloyed α -FAPbI₃ absorber, the champion solar cell achieved a PCE of 24.1%. Notably, the optimized device exhibited improved long-term stability, in which it operates at 85°C with the MPP tracking under 100 mW cm⁻² illumination for 1180 hours with ~1% loss of initial efficiency.

REFERENCES AND NOTES

- A. Kojima, K. Teshima, Y. Shirai, T. Miyasaka, *J. Am. Chem. Soc.* **131**, 6050–6051 (2009).
- H. Chen et al., *Science* **384**, 189–193 (2024).
- M. A. Green, A. Ho-Baillie, H. J. Snaith, *Nat. Photonics* **8**, 506–514 (2014).
- A. Polman, M. Knight, E. C. Garnett, B. Ehrler, W. C. Sinke, *Science* **352**, aad4424 (2016).
- N. Li, X. Niu, Q. Chen, H. Zhou, *Chem. Soc. Rev.* **49**, 8235–8286 (2020).
- T. A. S. Doherty et al., *Science* **374**, 1598–1605 (2021).
- T. Chen et al., *Sci. Adv.* **2**, e1601650 (2016).
- F. Cordero et al., *J. Phys. Chem. C Nanomater. Interfaces* **124**, 22972–22980 (2020).
- M. Kim et al., *Joule* **3**, 2179–2192 (2019).
- J. Liang et al., *Adv. Funct. Mater.* **32**, 2207177 (2022).
- Y. Zhang et al., *Adv. Energy Mater.* **11**, 2102538 (2021).
- H. Lu et al., *Science* **370**, eabb8985 (2020).

13. T. Niu *et al.*, *Adv. Mater.* **36**, 2309171 (2024).
14. T. Hou *et al.*, *Adv. Energy Mater.* **14**, 2407024 (2024).
15. J.-W. Lee *et al.*, *Nat. Commun.* **9**, 3021 (2018).
16. S. Sidhik *et al.*, *Science* **384**, 1227–1235 (2024).
17. Y. Wang *et al.*, *Adv. Energy Mater.* **14**, 2401721 (2024).
18. R. Hu *et al.*, *J. Mater. Chem. A Mater. Energy Sustain.* **8**, 8058–8064 (2020).
19. Z. Chen, G. Brocks, S. Tao, P. A. Bobbert, *Nat. Commun.* **12**, 2687 (2021).
20. L. Liu *et al.*, *Mater. Rep. Energy* **1**, 100064 (2021).
21. L. Shi *et al.*, *Science* **368**, eaba2412 (2020).
22. M. Wang *et al.*, *Nat. Energy* **8**, 1229–1239 (2023).
23. L. Chen *et al.*, *J. Am. Chem. Soc.* **145**, 27900–27910 (2023).
24. L. Chen *et al.*, *J. Am. Chem. Soc.* **146**, 10159–10166 (2024).
25. Z. Li *et al.*, *Nat. Commun.* **13**, 4417 (2022).
26. D. Lin *et al.*, *Adv. Funct. Mater.* **32**, 2208392 (2022).
27. T. Du *et al.*, *Adv. Mater.* **34**, 2107850 (2022).
28. S. Sánchez *et al.*, *Energy Environ. Sci.* **15**, 3862–3876 (2022).
29. J. Jeong *et al.*, *Nature* **592**, 381–385 (2021).
30. I. Turkevych *et al.*, *Nat. Nanotechnol.* **14**, 57–63 (2019).
31. Y. Zhang *et al.*, *Nat. Photonics* **17**, 1066–1073 (2023).
32. D. Lin *et al.*, *Small* **20**, e2307960 (2024).
33. H. Li *et al.*, *Sci. Adv.* **8**, eab07422 (2022).
34. K. Gjorgjevikj, M. Bukleski, S. Dimitrovska-Lazova, S. Aleksovska, *J. Mol. Struct.* **1293**, 136236 (2023).

35. A. A. Petrov *et al.*, *J. Phys. Chem. Lett.* **10**, 5776–5780 (2019).

36. C. Zhu *et al.*, *Nat. Commun.* **10**, 815 (2019).

ACKNOWLEDGMENTS

We thank J. Zhou (Peking University), F. Lin (Peking University), Y. Jiang (Peking University), X. Niu (Beijing Institute of Technology), and L. Li (North China Electric Power University) for their support in the discussions and characterizations. We thank the Materials Processing and Analysis Center, Peking University, for assistance with XRD and SEM characterization. **Funding:** This work was supported by the National Natural Science Foundation of China (52125206, 52433013, 22409008, 52022241 and 52402216), the Beijing Natural Science Foundation (Z240024), the National Key Research and Development Program of China (2023YFB4202502 and 2020YFB1506400), the China Postdoctoral Science Foundation (2024T170023), the Qing Lan Project, the Tencent Foundation through the Xplorer Prize, the China National Petroleum Corporation-Peking University Strategic Cooperation Project of Fundamental Research, the Sinopec Seeding Program, and the Yunnan Provincial Science and Technology Project at Southwest United Graduate School (202302A0370013). Part of the work was carried out at the Molecular Foundry and at beamline 12.3.2 at the Advanced Light Source, both user facilities supported by the Office of Science, Office of Basic Energy Sciences, of the US Department of Energy (contract no. DE-AC02-05CH11231 and DE-AC02-05CH11231).

Author contributions: Y. Zhang, Y.C., and H.Z. conceived the project. Y. Zhang and H.Z. supervised the project. Y. Zhang and Y.C.

prepared the samples, fabricated and characterized the devices, performed the stability test, analyzed the data, and wrote the first draft of the manuscript. G.L. and Y.W. contributed to the third-party certification of the devices' stability. Z.G. helped with the EL measurements. H.L. and K.L. helped with the fabrication of high-performance PSCs. Y. Zhao and T.K. conducted the GIWAXS measurements. Y. Zhang and Y.C. wrote the first draft of the manuscript. Y. Zhang, Q.C., and H.Z. revised the manuscript. All authors contributed to the discussion and commented on the manuscript. **Competing interests:** Authors declare that they have no competing interests. **Data and materials availability:** All data are available in the main text or the supplementary materials. **License information:** Copyright © 2025 the authors, some rights reserved; exclusive licensee American Association for the Advancement of Science. No claim to original US government works. <https://www.science.org/about/science-licenses-journal-article-reuse>

SUPPLEMENTARY MATERIALS

science.org/doi/10.1126/science.ads8968

Materials and Methods

Supplementary Text

Figs. S1 to S28

Table S1

References (37–47)

Submitted 3 September 2024; accepted 5 December 2024
10.1126/science.ads8968